

# Synthesis and characterization of $\text{Sm}^{3+}$ -doped ZnO nanoparticles via a sol–gel method and their photocatalytic application

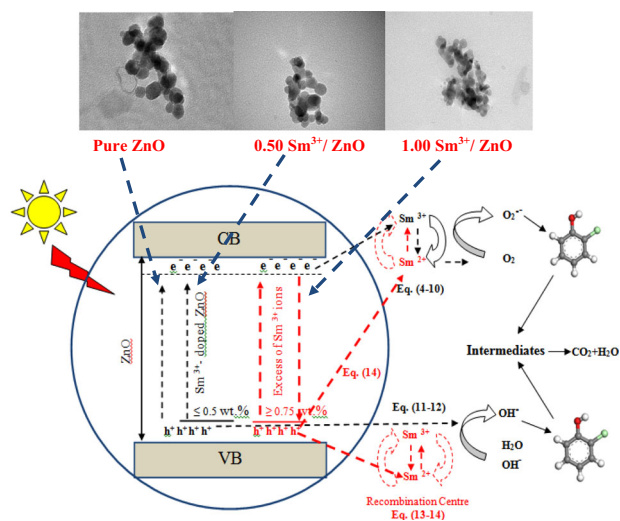
Muneer M. Ba-Abbad<sup>1,2,3</sup> · Mohd S. Takriff<sup>1,2</sup> · Abdelbaki Benamor<sup>4</sup> · Mustafa S. Nasser<sup>4</sup> · Ebrahim Mahmoudi<sup>1</sup> · Abdul Wahab Mohammad<sup>1,2</sup>

Received: 25 January 2017 / Accepted: 18 August 2017 / Published online: 7 September 2017  
© Springer Science+Business Media, LLC 2017

**Abstract** Spherical ZnO nanoparticles doped by samarium ions were successfully synthesized via a simple sol–gel method. The structures, morphologies, optical properties and surface areas were investigated for all samples using specific characterization methods. The hexagonal wurtzite structure of ZnO and samarium-doped ZnO nanoparticles were determined. The results obtained showed that the sizes of samarium-doped ZnO nanoparticles decreased with increasing samarium ion concentration. It was noticed that in the presence of samarium ions, the band gap slightly changed from the 3.198 eV of ZnO to 3.288 eV for samarium-doped ZnO with enhanced absorption in the UV region. This can be attributed to the transition of electrons from the conduction band to the acceptor energy level of samarium. The XPS results of samarium-doped ZnO, showed that only one oxidation state of samarium, with good incorporation into the ZnO matrix, was presented, with no peak of

samarium oxide. The surface areas analyses showed that higher surface areas were obtained for samarium-doped ZnO, which is attributed to the smaller size of the particles. The photocatalytic degradation of 2-chlorophenol was investigated under sunlight in presence of ZnO and samarium-doped ZnO nanoparticles. A higher performance of samarium-doped ZnO for photocatalytic degradation of 2-chlorophenol at 0.50 wt.% was observed, compared to pure ZnO nanoparticles under the same experimental conditions.

## Graphical abstract



**Electronic supplementary material** The online version of this article (doi:10.1007/s10971-017-4503-z) contains supplementary material, which is available to authorized users.

✉ Muneer M. Ba-Abbad  
muneer711@gmail.com

- <sup>1</sup> Department of Chemical and Process Engineering, Faculty of Engineering and Built Environment, Universiti Kebangsaan Malaysia, 43600 Bangi, Selangor, Malaysia
- <sup>2</sup> Research Centre for Sustainable Process Technology, Faculty of Engineering and Built Environment, Universiti Kebangsaan Malaysia, 43600 Bangi, Selangor, Malaysia
- <sup>3</sup> Department of Chemical Engineering, Faculty of Engineering and Petroleum, Hadhramout University of Science & Technology, Mukalla, Hadhramout, Yemen
- <sup>4</sup> Gas Processing Centre, Qatar University, P. O. Box 2713, Doha, Qatar

**Keywords**  $\text{Sm}^{3+}$ -doped · ZnO · Sol–gel · Photocatalytic

## 1 Introduction

Zinc oxide (ZnO) is an inorganic compound and an excellent alternative material of the II–VI semiconductor group.

Many properties of ZnO, such as electrical conductivity and optical properties make it a candidate for various applications. ZnO shows good potential for several applications such as in solar cells, laser diodes, gas sensors, and photocatalysis due to its wide band gap (3.37 eV) and its large exciting binding energy (60 mV) [1]. The piezoelectric property of ZnO indicates that it can be used for surface acoustic wave and electronic devices in several applications [2]. ZnO has three crystalline forms: hexagonal wurtzite, cubic zinc blended and the rarely observed cubic rock salt structure. The common and most stable structure of ZnO under ambient conditions is hexagonal wurtzite [3]. Generally, doping of ZnO has many advantages for controlling the size, shape, and surface of nanoparticles which could improve those materials in many applications [4]. Recently, control of the optical properties by reducing the particle size through doped impurity (ions) in the nano-crystals has been the focus of many studies [5]. The optical properties of ZnO, such as luminescence and absorbance due to excitonic recombination in the presence of an impurity have been widely reported [6]. However, many researchers have doped rare-earth ions into the ZnO lattice for specific applications in the ultraviolet (UV) and visible ranges [7]. The rare-earth-doped nanoparticles have been synthesized by several methods, such as hydrothermal [8], pulsed laser deposition [9], co-precipitation [10] and a sol–gel method [11]. In the last few years, many researchers have used the sol-gel method for the preparation of the metallic ion doped *n*-type semiconductors due to its lower equipment requirements and its cost effectiveness [12]. Additionally, some other advantages, including lower processing temperature, relative ease of introduction of dopants (even at a trace level) and easy adjustment of process conditions such as media pH [13]. In the last two years, samarium ( $\text{Sm}^{3+}$ )-doped ZnO with different shapes, such as spherical hierarchical nanostructures and nanorods have been reported [14, 15]. Furthermore, Khatamian et al. [16] have reported spherical nanoparticles (NPs) of  $\text{Sm}^{3+}$ -doped ZnO of larger size and higher agglomeration, which can influence their use and area of application. The main objective of this work is to prepare new  $\text{Sm}^{3+}$ -doped ZnO NPs with lower concentration of  $\text{Sm}^{3+}$  ions, which can provide solutions to the drawbacks mentioned in previous studies, and enhance the activity of degradation processes.

## 2 Experimental and method

### 2.1 Materials

Zinc acetate dihydrate ( $\text{ZnC}_4\text{H}_6\text{O}_4 \cdot 2\text{H}_2\text{O}$ ), purity 99.5%, obtained from Merck Chemical Company (Darmstadt, Germany) was used as the main source of ZnO NPs.

Absolute ethanol and oxalic acid ( $\text{C}_2\text{H}_2\text{O}_4$ ) with purity of 99.8 and 99.5% respectively, were supplied by R&M Chemicals, Malaysia. Samarium (III) nitrate ( $\text{Sm}(\text{NO}_3)_3 \cdot 6\text{H}_2\text{O}$ ), purity 99.9%, purchased from Sigma-Aldrich, was used throughout this work. 2-Chlorophenol (2-CP) with a purity of 98% was supplied by Merck. Deionised water was used to prepare all solutions.

### 2.2 Synthesis of samarium-doped ZnO nanoparticles

ZnO NPs were synthesized by simple sol–gel method without any addition of capping agent or surfactant. The optimum conditions to produce smaller-size ZnO NPs were a zinc acetate/oxalic acid molar ratio of 1:2 at a pH of  $2.0 \pm 0.2$  and a calcination temperature of  $400^\circ\text{C}$  as reported earlier [17, 18]. Zinc acetate was dissolved in ethanol under reflux with stirring at  $65^\circ\text{C}$ . Oxalic acid was dissolved in ethanol in a separate beaker and then slowly added to the zinc acetate solution. To prepare the  $\text{Sm}^{3+}$ -doped ZnO NPs, various amounts of  $\text{Sm}^{3+}$  ions: 0.25, 0.5, 0.75, and 1.0 wt%, were added to the first zinc acetate solution in ethanol and then oxalic acid solution added slowly. After 1 h stirring, the gel was formed and then dried at  $80^\circ\text{C}$  overnight. The final ZnO precursor powders were calcined at  $400^\circ\text{C}$  for 2 h.

### 2.3 Characterization of samarium-doped ZnO nanoparticles

Prepared samples of ZnO and  $\text{Sm}^{3+}$ -doped ZnO NPs were characterized using appropriate instruments needed for analysis of specific properties. Thermal decomposition was determined using thermogravimetric-differential scanning calorimetry (TGA-DSC) (model STA 449F3, Jupiter, Netzsch, Germany). The analysis was performed over a temperature range of  $30\text{--}800^\circ\text{C}$  with heating rate of  $10^\circ\text{C}/\text{min}$  with helium as carrier and nitrogen as a cooling gas. An X-ray diffraction (XRD) pattern was determined by X-ray diffractometer (D8 Advance Bruker AXS) at room temperature with Cu K $\alpha$  radiation ( $1.5406 \text{ \AA}$ ) in a  $2\theta$  scan range of  $20\text{--}80^\circ$  at a rate of  $0.2^\circ/\text{s}$  with accelerating voltage of 40 kV and emission current of 40 mA. The morphology and size of particles were evaluated by field emission scanning electron microscope (model SUPRA 55VP) and transmission electron microscope (model JEOLJEM 2100 at 200 kV) respectively. The optical properties such as band gap were determined by a Perkin Elmer LAMBDA 35 UV/Vis spectrophotometer at room temperature with wavelength ranging from 350 to 800 nm. The Brunauer–Emmett–Teller (BET) surface area was measured by nitrogen adsorption in a Micromeritics ASAP 2020 Accelerated Surface Area and Porosimetry System, USA. The average pore size was found from the desorption isotherm using the Barrett–Joyner–Halenda (BJH) method.

The energy binding and oxidation state of dopant ions were detected by X-ray photoelectron spectroscopy (XPS) using a KRATOS Axis Ultra DLD. The XPS analysis was carried out with monochromated Al K $\alpha$  (1486.6 eV) radiation as the excitation source at 15 kV.

## 2.4 Photocatalytic degradation of 2-CP and analysis

A cylindrical slurry batch reactor of 125 ml volume was used for 2-CP degradation tests. Degradation reaction of 2-CP was carried out from 12.00 a.m. to 2.00 p.m. at ambient temperature in presence of sunlight. A 50 mg/L initial concentration of 2-CP at pH of 6.0 was used for comparison between ZnO and Sm<sup>3+</sup>-doped ZnO NPs. The solution of 2-CP with a 1 g/l of ZnO and Sm<sup>3+</sup>-doped ZnO NPs was stirred in the dark for 0.5 h to achieve adsorption-desorption equilibrium before it was exposed to direct sunlight. After certain interval irradiation times, 1 ml samples of the 2-CP solution were collected, centrifuged and then filtered. These samples were analysed using high-performance liquid chromatography (HPLC) in an Agilent 1200 instrument equipped with a Jones LC-18 column (250 mm  $\times$  4.6 mm  $\times$  44  $\mu$ m) and a UV detector at 254 nm. An acetonitrile/water solution in a ratio of 20:80 v/v with 0.01 M phosphoric acid (H<sub>3</sub>PO<sub>4</sub>) was used as mobile phase at 1.0 ml min<sup>-1</sup> flow rate [19]. The degradation efficiency (DE %) for the removal of 2-CP at different interval times was calculated by Eq. 1:

$$\text{Degradation efficiency (DE\%)} = \frac{C_0 - C_t}{C_0} \times 100 \quad (1)$$

where  $C_0$  (mg/L) is the concentration of 2-CP at  $t = 0$  min, and  $C_t$  (mg/L) is its concentration at successive intervals of irradiation time.

All experiments of 2-CP degradation were carried out in sunny daylight conditions at ambient temperature. The UVA intensity of sunlight was measured for all experiments under similar conditions on sunny days. The average values were found to be almost constant with an average value of 23 W/m<sup>2</sup> over the entire experimental time. The UVA intensity of sunlight was measured by a Skyelynx type SDL 5100 instrument [20].

## 3 Result and discussion

### 3.1 Thermal analysis (DSC-TGA)

Thermal stability of pure ZnO and Sm<sup>3+</sup>-doped ZnO NPs was investigated over a temperature range of 30–800 °C. Figure 1 shows the TGA-DSC curves for both ZnO and Sm<sup>3+</sup>-doped ZnO precursors prepared under the same conditions. From the TGA-DSC curves, two endothermic

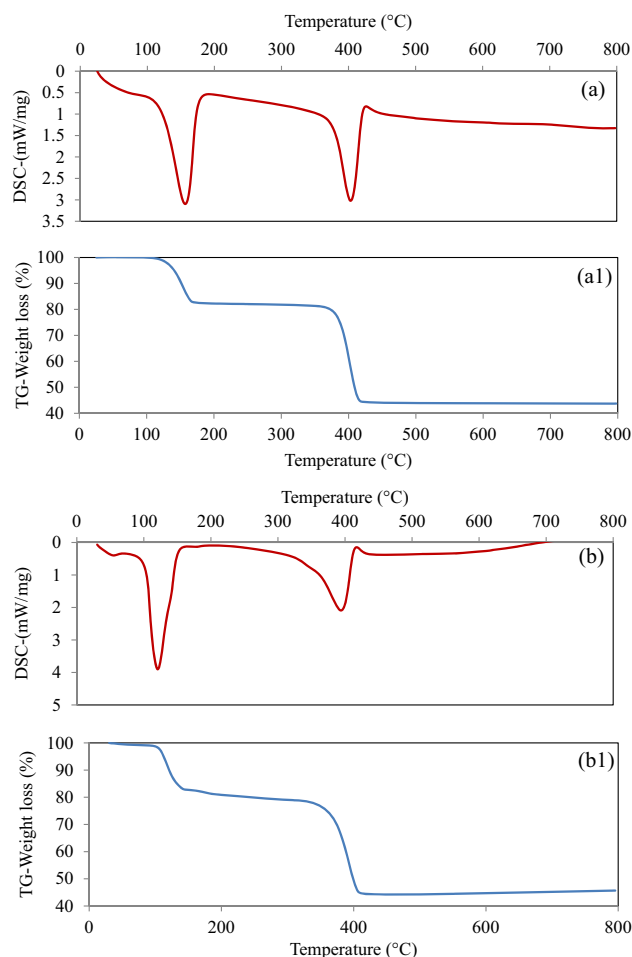


**Fig. 1** DSC-TGA curves of **a, a1** pure ZnO, **b, b1** 0.5 wt.% Sm<sup>3+</sup>-doped ZnO

peaks for the ZnO and three peaks for Sm<sup>3+</sup>-doped ZnO were observed in the heating profile, with a corresponding loss of weight. The first peak, which is the smallest, appeared at temperature range 50 to 75 °C for the Sm<sup>3+</sup>-doped ZnO sample. It is attributed to the loss of ethanol which increased by doping ions due to the nature of the material used for doping. This peak may be due to presence of ethanol in the structure of the Sm<sup>3+</sup>-doped ZnO sample which needed more time to release it and dried compared to the pure ZnO sample. Water removal was observed between 100 and 140 °C as the second peak for both samples. Additionally, a third small peak appeared before 190 °C in the Sm<sup>3+</sup>-doped ZnO sample, which is attributed to the release of nitrate (precursor of dopant) as nitrogen oxide. The final peak could be attributed to the thermal decomposition of oxalate to ZnO NP for both samples.

The TGA curves revealed that four different weight losses occurred during the complete thermal decomposition. Weight loss of ZnO and Sm<sup>3+</sup>-doped ZnO NPs were calculated and listed in Table 1. The temperature range was

**Table 1** Weight loss (%) of ZnO and Sm<sup>3+</sup>-doped ZnO precursors under temperatures profile

Material/temperature range	50–75 °C	100–140 °C	140–200 °C	200–420 °C
ZnO	–	17.9%	–	36.10%
0.5 wt.% Sm <sup>3+</sup> -doped ZnO	2.1%	18%	2%	36.57%

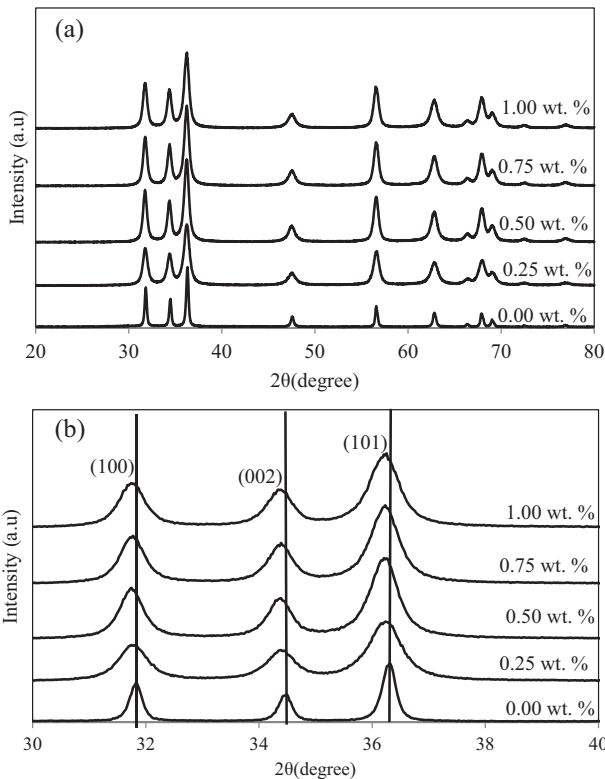


**Fig. 2** XRD patterns spectrum of **a** Sm<sup>3+</sup>-doped ZnO NPs with different concentration calcined at 400 °C **b** shifted of peak (101) position is observable towards to left side

divided into four segments according the DSC curve. The first segment is related to ethanol loss which chelates or bonds with a carboxyl group (COOH) during the reaction of oxalic acid with zinc acetate. The weight loss during the second range, occurring between 100 and 140 °C, is due to dehydration of the oxalate (anhydrous zinc oxalate). The third weight loss, occurring at 140 to 200 °C, is very close to the results obtained using samarium nitrate as a precursor of Sm<sup>3+</sup> doping source with no loss of ZnO [20].

The final weight loss of ZnO and Sm<sup>3+</sup>-doped ZnO NPs, occurring between 200 and 420 °C is due to decomposition of zinc oxalates dihydrates before and after the doping operation. The largest weight loss was obtained by the decomposition of anhydrous zinc oxalate to ZnO before and after the doping as shown in Fig. 1 and summarized in Table 1. These results of ZnO and Sm<sup>3+</sup>-doped ZnO are in good agreement with the theoretical results reported recently [21]. The difference in weight loss between the ZnO and Sm<sup>3+</sup>-doped ZnO NPs is due to the thermal

**Table 2** Crystal size, lattice parameters, and band gap of ZnO and Sm<sup>3+</sup>-doped ZnO NP with various concentrations of Sm<sup>3+</sup>

Concentration of Sm <sup>3+</sup> (wt.%)	Crystal size (nm)	Lattice parameters a = b (nm)	Lattice parameters c (nm)	Band gap (eV)
0.00	18.9	0.3248	0.5205	3.198
0.25	15.8	0.3250	0.5207	3.282
0.50	13.6	0.3250	0.5207	3.283
0.75	13.0	0.3253	0.5213	3.287
1.00	12.7	0.3253	0.5213	3.288

decomposition of the additive of doping ions and is close to ≈0.5 wt.%.

### 3.2 X-ray diffraction analysis (XRD)

Figure 2 shows the XRD patterns of ZnO and Sm<sup>3+</sup>-doped ZnO NPs with various concentrations of Sm<sup>3+</sup> ions in the scan range of 2θ from 20 to 80°. All XRD peaks of samples were checked using a standard JCPDS card No. 36–1451, which confirms a wurtzite structure with a hexagonal phase and the P63mc space group. The effect of Sm<sup>3+</sup> concentrations of 0.25 to 1.0 wt% on the crystal size of ZnO were investigated. The XRD patterns of the dopant samples indicated that the doping occurs without any change in the phase structure of the ZnO NP as shown in Fig. 2a. It is also noticeable that no peak for samarium oxide (Sm<sub>2</sub>O<sub>3</sub>) appears in the diffraction spectrum, which confirms that doping occurred in the unit cell of ZnO [22]. However, when the Sm<sup>3+</sup> concentration increased, the intensities of the peaks decreased and became broader compared to those of pure ZnO. In addition, the diffraction peaks of Sm<sup>3+</sup>-doped ZnO became broader and weaker in intensity with increasing Sm<sup>3+</sup> concentration due to the Sm<sup>3+</sup> doping ions inhibiting crystal growth.

The average crystal sizes (*D*) and inter-planer spacing (*d*-value) were calculated from the Debye–Scherer equation (Eq. 2) [23]:

$$D = \frac{K\lambda}{\beta \cos \theta} \text{ and } d = \frac{\lambda}{2 \sin \theta} \tag{2}$$

where *K* is the Scherer constant (*K* = 0.89),  $\lambda$  is the incident X-ray wavelength,  $\beta$  is the peak width at half maximum and  $\theta$  is the Bragg diffraction angle. These results confirm the occurrence of doping of Sm<sup>3+</sup> into the ZnO crystal lattice as given in Table 2. These phenomena can be attributed to the

**Table 3** Measured and calculated d spacing values of ZnO and Sm<sup>3+</sup>-doped ZnO NP with various concentrations of Sm<sup>3+</sup>

Value of d spacing (nm) measured using XRD software									
0.00 wt. %		0.25 wt. %		0.50 wt. %		0.750 wt. %		0.00 wt. %	
2θ	ds	2θ	ds	2θ	ds	2θ	ds	2θ	ds
31.812	0.281074	31.763	0.281495	31.757	0.281542	31.746	0.281639	31.735	0.281736
34.448	0.260145	34.381	0.260631	34.378	0.260653	34.375	0.260677	34.358	0.260804
36.287	0.247369	36.222	0.247798	36.221	0.247800	36.219	0.247810	36.190	0.247817
Value of d spacing (nm) calculated using Eq.(2)									
31.812	0.281069	31.763	0.281492	31.757	0.281544	31.746	0.281639	31.735	0.281734
34.448	0.260141	34.381	0.260633	34.378	0.260655	34.375	0.260677	34.358	0.260802
36.287	0.247368	36.222	0.247797	36.221	0.247803	36.219	0.247817	36.190	0.248009

differences in ionic radii of the Zn<sup>2+</sup> (0.074 nm) and Sm<sup>3+</sup> (0.096 nm) ions [16]. The Sm<sup>3+</sup> appears easily incorporated into the ZnO NP matrix due to the lattice disorder and associated to stresses of the ZnO cell during the doping process as reported earlier [24]. The doping of Sm<sup>3+</sup> into the ZnO lattice caused shifting of peaks at (100), (002), and (101) to the left (lower value of 2θ) with increasing Sm<sup>3+</sup> concentration, as shown in Fig. 2b. These results showed that Sm<sup>3+</sup> ions substituted for Zn<sup>2+</sup> in the matrix of ZnO which caused changes in the inter-planar spacing (ionic radius of Sm<sup>3+</sup> is larger than that of Zn<sup>2+</sup>).

The values of inter-planar spacing were calculated using the planes (100), (002), and (101) from XRD data in Fig. 2b at 2θ of 31.81°, 34.44°, and 36.28° for pure ZnO. The results of measured and calculated inter-planar spacing using XRD software and Eq. 2 were summarized in Table 3. These values of Sm<sup>3+</sup>-doped ZnO become slightly bigger compared with ZnO which confirmed the Sm<sup>3+</sup> doing into the ZnO cell with changed of crystal size and shifting of ZnO peaks to lower 2θ. However, the calculated values was observed in good agreement with measured which supported the accurately of the results. These values showed distortion of ZnO after doping with variation of bond length and bond angles between atoms caused changes of the lattice strain and planes. By increases of tensile stress, the d-value of spacing causes of peaks shifting to lower 2θ values [24]. In general, doping using rare-earth ions have been reported to restrain the growth of ZnO crystals. However, the doping of ZnO by Sm<sup>3+</sup> ions decreases of crystal size which is attributed to the formation of Sm–O–Zn, inhibiting the crystal growth [24]. The successful incorporation of Sm<sup>3+</sup> ions into the ZnO cell were also verified by XPS analysis.

### 3.3 Surface morphology

The morphology and size of Sm<sup>3+</sup>-doped ZnO NPs were investigated using field emission scanning electron microscopy (FESEM) and transmission electron microscopy

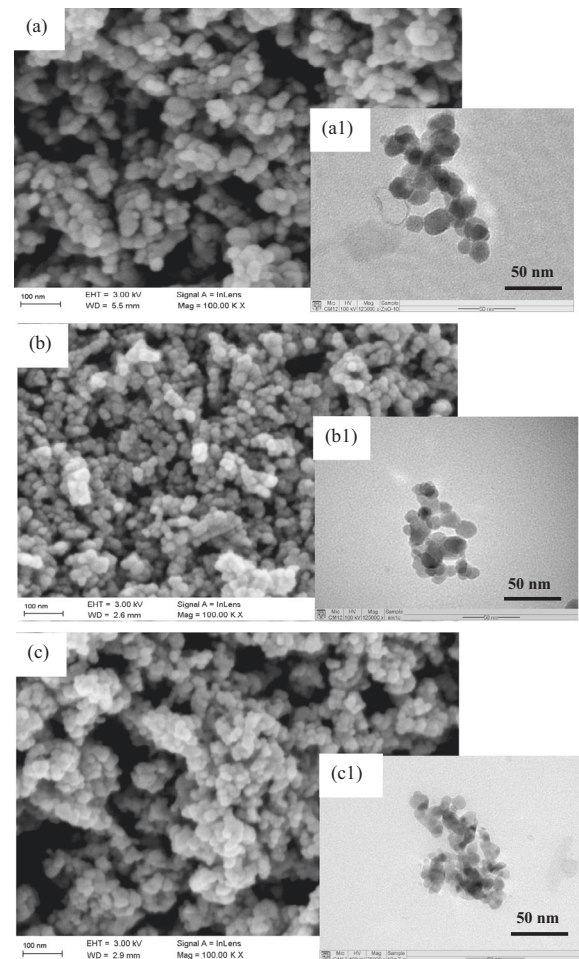


**Fig. 3** FESEM and TEM images of **a, a<sub>1</sub>** ZnO; **b, b<sub>1</sub>** 0.5 wt.%; **c, c<sub>1</sub>** 1.00 wt.% of Sm<sup>3+</sup>-doped ZnO NPs

(TEM) under higher magnification and compared with pure ZnO NPs as shown in Fig. 3. To assess the influence of doping on ZnO morphology, samples with average and higher concentrations were selected for the analyses. Concentrations of Sm<sup>3+</sup> ions varying between 0.25 and 1.0 wt.

**Table 4** Surface area of ZnO and Sm<sup>3+</sup>-doped ZnO samples

Concentration of Sm <sup>3+</sup> (wt.%)	Crystal size (nm)	Surface area (m <sup>2</sup> /g)	Pore volume (cm <sup>3</sup> /g)	Average pore size (nm)
0.00	18.00	26	0.1261	25.39
0.25	15.80	27	0.1413	23.99
0.50	13.60	30	0.1592	22.77
0.75	13.00	32	0.1760	21.50
1.00	12.70	34	0.2244	21.09

% were used to investigate the effects of the dopant on the morphology and the particle size of ZnO NPs. The FESEM and TEM images reveal that the shapes of ZnO and Sm<sup>3+</sup>-doped ZnO particles were mostly spherical with a uniform size distribution. However, a significant aggregation of ZnO particles was observed as compared to Sm<sup>3+</sup>-doped ZnO samples.

It was worth noting that all ZnO NPs doped by Sm<sup>3+</sup> ions with concentrations varying from 0.5 to 1.00 wt.% exhibited less aggregation than did pure ZnO NPs. As shown in the TEM images, the particle size of the Sm<sup>3+</sup>-doped ZnO decreased as the concentration of the doping ions increased. Upon further increase of the ion concentration from 0.25 to 1.00 wt.%, the average particle size decreased from 20 to 12 ± 2 nm, which is consistent with the results obtained by XRD analysis. The observed slight agglomeration of Sm<sup>3+</sup>-doped ZnO samples is attributed to the aggregation of small particles formed after the doping process, as reported by Tseng et al. [25]. In fact, the generally high surface area to volume ratio of nanoparticles provides a very high surface energy which caused agglomeration of the nanoparticles, which is commonly observed in nanopowders [26]. However, it is impossible to avoid agglomeration even in the presence of surfactants during the process [27]. The aggregation of nanoparticles reduces the surface energy and makes the nanoparticles more stable, especially when not using any capping agent or surfactant to modify their surface [28]. In this study, no capping agent or surfactant was used so the surface properties were influenced by the size and aggregation and agglomeration of these particles. The Sm<sup>3+</sup>-doped ZnO samples showed that many smaller particle (12 ± 2 nm, Figs. 3, b, c) aggregated to become more stable (lower surface energy) which avoid agglomeration, compare to pure ZnO. This phenomenon, of reducing the agglomeration by reducing the particle size has been reported earlier [29]. Furthermore, the Sm<sup>3+</sup>-doped ZnO samples with concentration of more than 0.5 wt.% produced higher surface area, especially at 1.0 wt.%, due to the aggregation of smaller particles to reduce the pore size between them, as shown in Fig. 3 and Table 4.

### 3.4 Surface area analysis

Generally, the surface area of a nanocatalyst is one of the important characteristics that affects its quality and activity within a process. The BET method is considered to be the most useful method to measure the surface area, and is based on the theoretical model of a monolayer formation in the physical adsorption of gas molecules [30]. Figure 4 shows the nitrogen adsorption-desorption isotherms of all ZnO NP samples doped with Sm<sup>3+</sup> ions with concentration varying between 0.25 and 1.0 wt.%. Sm<sup>3+</sup>-doped ZnO NP samples exhibit type V adsorption-desorption isotherms according to the IUPAC classification. Additionally, the H1 hysteresis loops based on the IUPAC classification were found to be in the range of 0.8 to 0.99 [30]. All surface properties, such as surface area, pore volume and average pore size of Sm<sup>3+</sup>-doped ZnO NP samples are given in Table 4 and compared with their corresponding values of the pure ZnO samples. It is noticeable that with increased concentrations of Sm<sup>3+</sup> ions, the volume of adsorbed gas increased and the hysteresis loops became broader under a range of relative pressure varying from 0.8 to 0.99. These results are attributed to the increased surface area with increased ion concentration [31].

From Table 4 it can be observed that for all concentrations of Sm<sup>3+</sup>-doped ZnO NPs, the surface areas are higher compared to those of pure ZnO. This result confirms that the doping process enhances the surface area of ZnO NPs, even at low concentrations [31]. The pore sizes were measured by the BJH method, and the average pore sizes obtained for both ZnO and Sm<sup>3+</sup>-doped ZnO NPs were decreased from 25.20 to 21.50 nm, respectively. The average pore sizes of all samples were less than 50 nm, which confirms that all samples are of mesopore (2–50 nm) type as reported earlier [32]. These results show that the larger surface area of Sm<sup>3+</sup>-doped ZnO NPs is attributed to the smaller particles size, as was confirmed by the XRD and TEM analyses.

### 3.5 Optical properties

The optical properties, such as band gap of ZnO and Sm<sup>3+</sup>-doped ZnO NPs were determined. The band gap of the ZnO and Sm<sup>3+</sup>-doped ZnO NPs with concentration of 0.25 to 1.0 wt.% was investigated by UV-Vis measurement using the absorbance spectrum between 200 and 800 nm (Fig. 5a). The band gap of all samples was calculated by applying of absorption data in Eq. (3) below [33]:

$$\alpha h\nu = E_d(h\nu - E_g)^{\frac{1}{2}} \quad (3)$$

where  $\alpha$  is the optical absorption coefficient,  $h\nu$  the photon energy,  $E_g$  the direct band gap, and  $E_d$  is constant. By

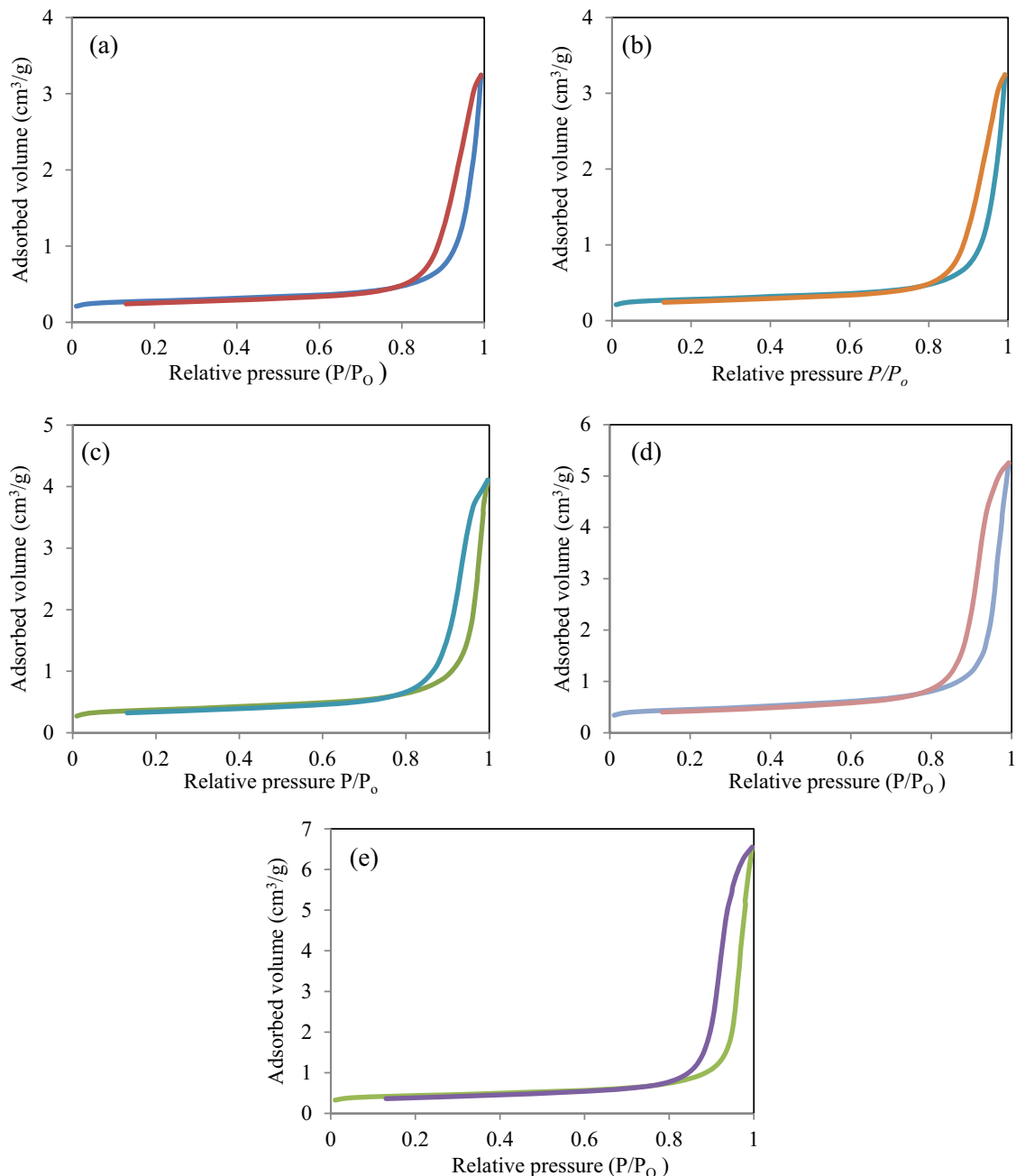


**Fig. 4** Nitrogen adsorption-desorption of ZnO and doped ZnO NP with various  $\text{Sm}^{3+}$  ions **a** 0.00 wt.%, **b** 0.25 wt.%, **c** 0.50 wt.%, **d** 0.75 wt.%, **e** 1.00 wt.%

plotting  $(\alpha h\nu)^2$  as a function of photon energy and extrapolating the linear portion of the curve to zero, the value of the band gap ( $E_g$ ) of the samples can be obtained at different conditions from Fig. 5b. The ZnO NP spectrum indicates an absorption onset at approximately 390 nm, and the intrinsic energy band gap of ZnO was 3.198 eV which is in good agreement with an earlier study [33]. Band gap energies of between 3.282 and 3.288 eV were obtained for concentrations of 0.25 to 1.0 wt.%, as given in Table 2. A slight blue shift in the absorbance (i.e., an increase in the band gap) for

the  $\text{Sm}^{3+}$ -doped ZnO samples was observed with an increase in the concentration of  $\text{Sm}^{3+}$  ions, as reported earlier [34]. Increases in the band gap with the blue shift were attributed to the shift of Fermi levels close to the conduction band, resulting in an increase in the carrier concentration, which blocks low-energy transitions according to the Burstein–Moss effect [35]. The band gaps of  $\text{Sm}^{3+}$ -doped ZnO were shifted to blue which is due to different crystal size and to the morphologies of ZnO NPs before and after doping. Hence, the doping of ZnO by  $\text{Sm}^{3+}$

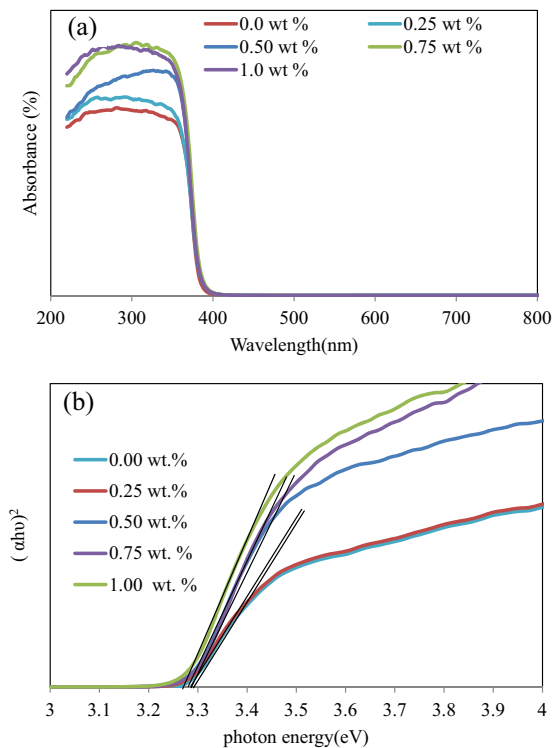


**Fig. 5** Optical properties of ZnO and Sm<sup>3+</sup>-doped ZnO NPs **a** Absorbance **b** band gap determination

ions has enhanced absorption in the UV region rather than the visible, as reported previously [36].

### 3.6 XPS analysis

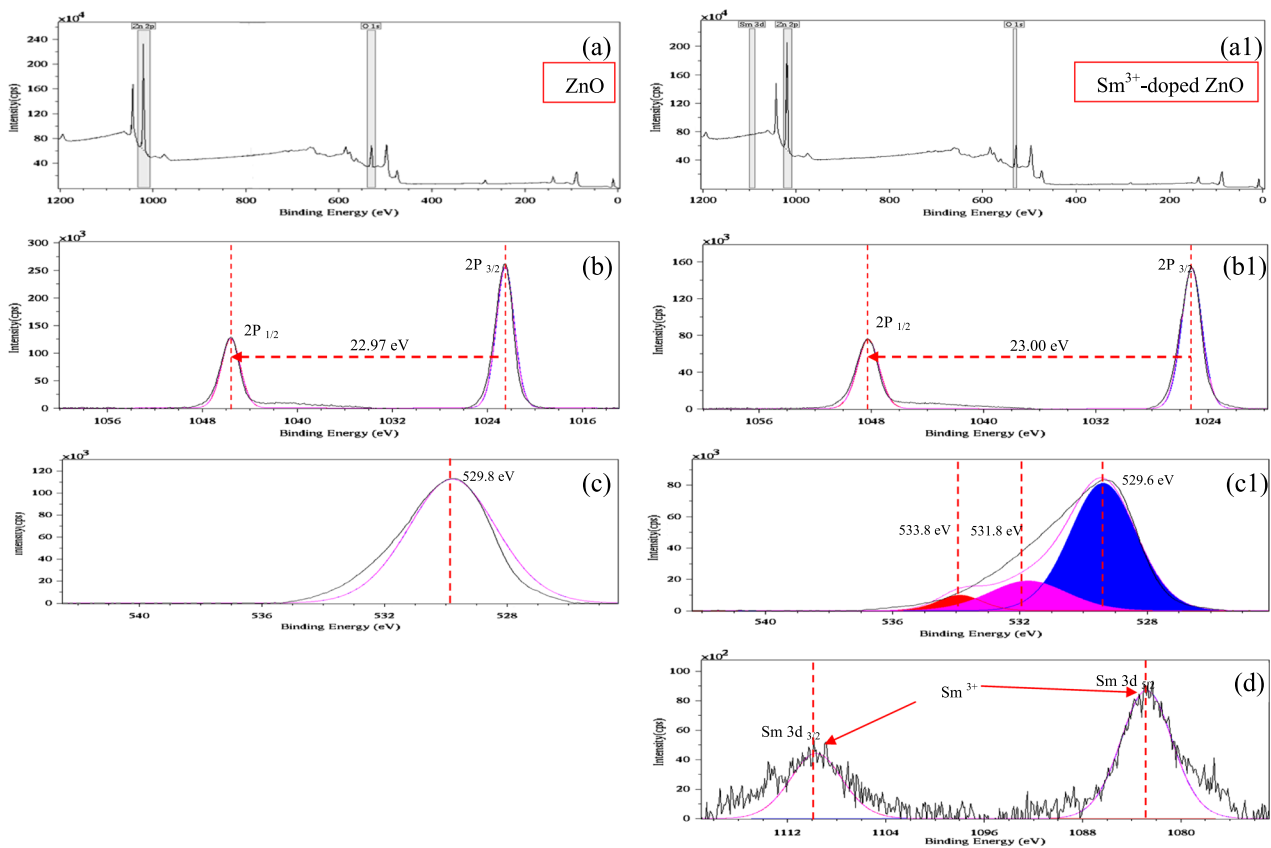
The chemical compositions of ZnO and Sm<sup>3+</sup>-doped ZnO NPs (0.5 wt.%) were investigated by XPS analysis as shown in Fig. 6. The chemical characterization includes the determination of element valences based on their binding energies. Figure 6a, a1 shows the spectrum of the ZnO and Sm<sup>3+</sup>-doped ZnO NP (0.5 wt.%) sample, which includes mainly oxygen (O1<sub>s</sub>), samarium (Sm<sup>3+</sup>), zinc species (Zn 3<sub>p</sub>) and carbon (C1<sub>s</sub>). The reference of XPS analysis calibrate using carbon peak (C 1s) which binding energy was 284.8 eV. For ZnO, two peaks at 1022.50 eV and 1045.50 eV for zinc as Zn 2p were observed which indicate binding energies of Zn 2p 3/2 and Zn 2p 1/2 (Fig. 6b). These peaks confirm the emission by ZnO by 2p photoelectrons as reported earlier [37]. Between the two peaks, the energy difference was about 23 eV, which is in good agreement with the standard value of 22.97 eV (≈23.0 eV) for Zn<sup>2+</sup> ions in the oxide as previously reported [37]. Furthermore, the binding energies of Zn 2p 3/2 and Zn 2p 1/2 for the Sm<sup>3+</sup>-doped ZnO NP sample shifted to higher (increased) to ≈1025.50 and 1048.25 eV, respectively, as shown in Fig. 6b1. This shifting in binding energies confirm that

electronic interaction between the ZnO and the Sm<sup>3+</sup> dopant which is main responsible for the enhancement of degradation process. Figures 6c, c1 shows the peak fitting of O 1s for ZnO and Sm<sup>3+</sup>-doped ZnO NPs which found at 529.8 and 529.6 eV, respectively. The lower binding energy of the O 1s are may be attributed to the coordination of oxygen in Zn–O in both samples of ZnO and Sm<sup>3+</sup>-doped ZnO NPs. Two other peaks presence in Sm<sup>3+</sup>-doped ZnO NPs as shown in Fig. (c1). The first peak at higher energy of 531.8 eV is assigned to the O<sup>−</sup> as the oxygen vacancies and the second at 533.8 eV corresponds to the hydroxyl species (OH) from adsorbed water on the surface of Sm<sup>3+</sup>-doped ZnO NP [37]. As shown in Fig. 6 (d), one oxidation state of samarium, Sm<sup>3+</sup> was observed in the XPS spectrum of Sm<sup>3+</sup>-doped ZnO NPs. The two peaks of binding energy for Sm<sup>3+</sup> were assigned to Sm<sup>3+</sup> 3d 5/2, 3/2 at 1083 and 1110 eV, respectively, in agreement with the values reported in a previous work [38]. No peak of other samarium valence, such as Sm<sup>2+</sup> or samarium oxide (Sm<sub>2</sub>O<sub>3</sub>) was detected in the XPS spectra, as was reported earlier [39]. The fact that the Sm<sup>3+</sup> ions were detected only as trivalent in the Sm<sup>3+</sup>-doped ZnO NP sample confirms the incorporation of Sm<sup>3+</sup> ions into the ZnO matrix. These results indicate that all Sm<sup>3+</sup> ions are incorporated into the ZnO lattice without any segregation of Sm<sub>2</sub>O<sub>3</sub> oxide phase which is in accordance with XRD analysis

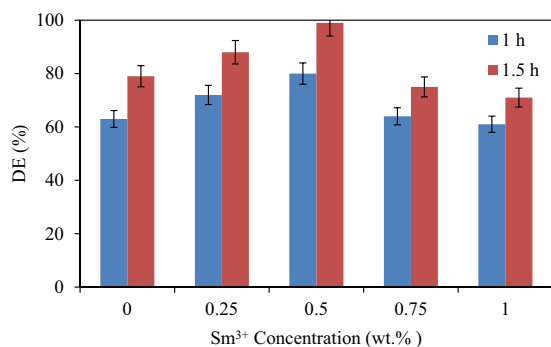
### 3.7 Activity of samarium-doped ZnO nanoparticles for 2-CP degradation

Figure 7 shows the degradation efficiency of 2-CP using Sm<sup>3+</sup>-doped ZnO with several concentrations of Sm<sup>3+</sup> under different irradiation times and compared to pure ZnO NPs. All experiments of 2-CP degradation were repeated three times under the same initial condition of 2-CP concentration 50 mg/l with catalyst loading of 1 g/l for 1 and 1.5 h irradiation times. Observing the Sm<sup>3+</sup> concentration increase up to 0.5 wt.% (as optimum), the degradation increased to a maximum value and then declined as Sm<sup>3+</sup> concentration exceeded that optimal value. The degradation efficiency of 0.5 wt.% Sm<sup>3+</sup>-doped ZnO was 80%, higher than the 63% value shown by ZnO using the same amount of catalyst loading (1 g/l) within 1 h. The highest degradation efficiency of 99% was obtained using 0.50 wt.% Sm<sup>3+</sup>-doped ZnO for 1.5 h irradiation time with same catalyst amount as shown by the HPLC results (see supplementary file). This result is confirmed by the decline of the main peak of 2-CP to its lowest within 1.5 h, compared to 1 h, confirming that the highest efficiency was achieved at 1.5 h irradiation time. This may be due to the enhancement of absorbance to slightly visible for Sm<sup>3+</sup>-doped ZnO. The increased surface area of Sm<sup>3+</sup>-doped ZnO compared to that of ZnO does not always lead to a higher efficiency. A





**Fig. 6** XPS spectra of ZnO and Sm<sup>3+</sup>-doped ZnO NP: **a, a1** XPS survey spectra **b, b1** Region of Zn 2p, **c, c1** Region of O 1s, **d** Sm 3d of Sm<sup>3+</sup>-doped ZnO

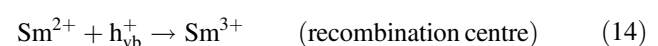
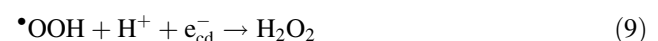
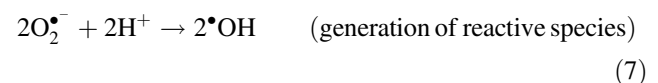
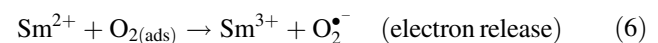
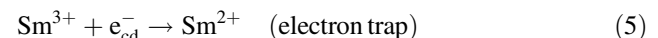
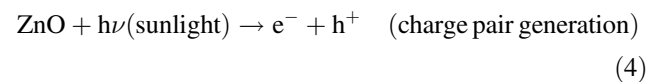


**Fig. 7** Comparison of photocatalytic degradation efficiency of 2-CP vs. the different concentration of Sm<sup>3+</sup> ions doped ZnO (with standard Error)

small amount of Sm<sup>3+</sup> ions (0.50 wt.%) clearly enhances the activity of ZnO particles, which may be due to an increase in the separation of the photo-generated electrons and the photo-generated hole traps [40].

To generate oxidative species, such as the superoxide radical ion (O<sub>2</sub><sup>•-</sup>), the Sm<sup>3+</sup> ions present on the ZnO surface need to react with the electrons that are transferred to the oxygen molecules and the explanation given by the reaction

mechanism below:



The active  $\cdot\text{OH}$  species could be generated at  $h\nu_{\text{vb}}^+$  by adsorption of  $\text{H}_2\text{O}$  or  $\text{OH}^-$  on the surface of  $\text{Sm}^{3+}$ -doped ZnO according to the steps given in Eqs. 11 & 12. The electron-hole recombination is faster in the presence of  $\text{Sm}^{3+}$  ions, due to the unstable  $\text{Sm}^{2+}$  ions that can easily transfer electrons to the oxygen molecules. This is possible because the partially filled f-orbital (strong Lewis acid) in  $\text{Sm}^{3+}$ -doped ZnO can trap the  $e_{\text{cd}}^-$  and stop the recombination by  $h\nu_{\text{vb}}^+$ . However, the  $\text{Sm}^{2+}$  state with six unstable electrons easily causes a release of  $e_{\text{cd}}^-$  to produce  $\text{O}_2^{\cdot-}$  then  $\cdot\text{OH}$  [41]. When the concentration of  $\text{Sm}^{3+}$  ions is higher than the optimal value (i.e.,  $>0.5 \text{ wt.}\%$ ), a decrease in the

catalyst activity was observed. This could be attributed to the excess  $\text{Sm}^{3+}$  working as a recombination centre as illustrated in Eqs. 13 & 14. By increasing the  $\text{Sm}^{3+}$  generation in the valence band (Eqs. 13 & 14), a higher possibility to react with excess  $e_{\text{cd}}^-$  in the conduction band to produced  $\text{Sm}^{2+}$  (Eq. 5) was observed. More unstable  $\text{Sm}^{2+}$  ions can be easily transferred to  $h\nu_{\text{vb}}^+$  to form  $\text{Sm}^{3+}$  (Eq. 14) which could delay this cycle of other reactions (Eqs. 6, 7, 11, 12, 13) and cause a decrease of degradation efficiency. These reactions have the effect of reducing the photocatalytic activity of  $\text{Sm}^{3+}$ -doped ZnO when the optimal concentration was exceeded ( $0.50 \text{ wt.}\%$ ). The mechanism to

**Fig. 8** Proposed mechanism for the photocatalytic degradation of 2-CP on  $\text{Sm}^{3+}$ -doped ZnO NP (black row is enhanced of degradation, red rod is inhibition of degradation)

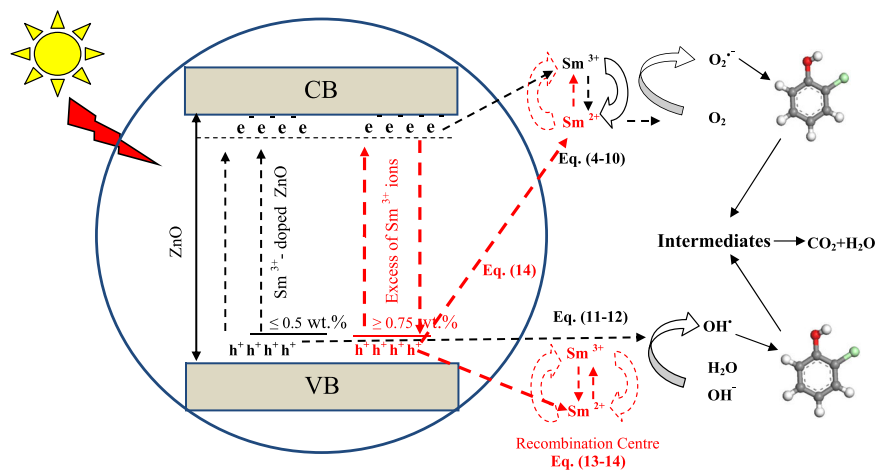


**Table 5** Comparison of the  $\text{Sm}^{3+}$ -doped ZnO NP and other different spherical oxides for 2-CP degradation with their optimum conditions

Photocatalyst type	Concentration (mg/l) of 2-CP	Amount (g/l) Photo-catalyst	Solution pH	light Source	degradation efficiency % (Time by hour)	Ref.
ZnO (C)	50	2	6	sunlight	98 (2.5 h)	[42]
ZnO: TiO <sub>2</sub> (P)	25	3	9	UV	97 (3 h)	[43]
TiO <sub>2</sub> (P)	65	6	10.7	UV	97.30 (6.5 h)	[44]
TiO <sub>2</sub> /Clay (P)	190	1.5	-	UV	100 (10 h)	[45]
TiO <sub>2</sub>	50	1	5	UV	50.5 (3 h)	[46]
InVO <sub>4</sub> /TiO <sub>2</sub> (P)	50	1	5	UV	100 (3 h)	[46]
Fe <sub>3</sub> O <sub>4</sub> /SiO <sub>2</sub> /TiO <sub>2</sub> (P)	50	0.5	3	UV	97 (3 h)	[47]
CeO <sub>2</sub> (P)	200	3.3	-	UV	97 (24 h)	[48]
ZrO <sub>2</sub> (P)	200	3.3	-	UV	97 (24 h)	[48]
$\alpha$ Fe <sub>2</sub> O <sub>3</sub> (P)	65	1.5	6	UV	80 (24 h)	[49]
ZnO(P)	50	1	6	sunlight	80 (1.5 h)	This study
$\text{Sm}^{3+}$ /ZnO(P)	50	1	6	sunlight	99 (1.5 h)	This study
$\text{Sm}^{3+}$ /ZnO(P)	100	1	6	sunlight	70 (1.5 h)	This study
$\text{Sm}^{3+}$ /ZnO(P)	150	1	6	sunlight	64 (1.5 h)	This study

C commercial, P prepared

enhance photocatalytic degradation by  $\text{Sm}^{3+}$ -doped ZnO in presence of optimum and excess  $\text{Sm}^{3+}$  ion concentration by combining the results of our experiments and previous studies [13, 14, 41] is proposed in Fig. 8.

Ultimately, the performance of prepared ZnO and  $\text{Sm}^{3+}$ -doped ZnO NPs (optimum value 0.50 wt.%) in the degradation of 2-CP can be summarized and compared with other previously reported results using different photocatalysts included in ZnO. Table 5 shows the performance of spherically shaped ZnO and some other oxides being applied to 2-CP degradation in aqueous solution, along with the conditions used. In general, these results show that  $\text{Sm}^{3+}$ -doped ZnO NPs exhibit a good performance activity compared to other oxides, either single or as composites, which needed more time to achieve higher degradation efficiency, with higher amount of catalyst loading, compared to this study. For a single photocatalyst such as  $\text{TiO}_2$  (Table 5), to achieve higher degradation efficiency required more irradiation time or increased loading. However, the degradation efficiency can be improved by combining more than one photocatalyst or composite, such as  $\text{InVO}_4/\text{TiO}_2$  and  $\text{Fe}_3\text{O}_4/\text{SiO}_2/\text{TiO}_2$ , as reported in Table 5. However, higher performance of  $\text{Sm}^{3+}$ -doped into ZnO NP under same experimental conditions were obtained for concentrations 100 to 150 mg/l of 2-CP degradation within 1.5 h, as given in Table 5.

In other studies, different shapes of  $\text{Sm}^{3+}$ -doped ZnO photocatalysts have been synthesized to degrade different pollutants [13]. The  $\text{Sm}^{3+}$ -doped ZnO with a nanorod shape was applied to degrade 20 mg/l of phenol with 2 g/l loading and achieved an efficiency of 95.9% within 8 h [13]. The  $\text{Sm}^{3+}$ -doped spherical-like ZnO hierarchical was used to remove 20 mg/l of 2,4-dichlorophenol from aqueous solution with 3 g/l of loading, and 95% of degradation efficiency was obtained after 3 h [14]. In addition, spherical  $\text{Sm}^{3+}$ -doped ZnO was used to treat 10 mg/l of 4-nitrophenol at 1 g/l loading, in which 58% degradation efficiency was achieved within 3.25 h [16]. In conclusion, this study presents a low cost method for the preparation of high performance  $\text{Sm}^{3+}$ -doped ZnO catalysts for application in the treatment of toxic compounds in water under the environmental friendly source of sunlight (no cost) which is worth focusing in future research for wider applications.

## 4 Conclusion

Free of any use of capping agents or surfactants, spherical  $\text{Sm}^{3+}$ -doped ZnO NPs were prepared successfully by a simple sol-gel route. Several  $\text{Sm}^{3+}$  ion concentration were used and properties confirmed by TGA, XRD, FESEM, TEM, BET, UV-Vis, and XPS analysis. These characterizations confirmed that  $\text{Sm}^{3+}$  ions were doped successfully

into the unit cell of the ZnO NPs and modified their properties. The activity of ZnO and  $\text{Sm}^{3+}$ -doped ZnO NPs for the photocatalytic degradation of 2-CP under sunlight were compared. The highest degradation efficiency of 99% was shown by 0.50 wt %  $\text{Sm}^{3+}$ -doped ZnO compared to 80% for pure ZnO with 1 g/l loading and 1.5 h irradiation time. The enhancement of photocatalytic degradation of  $\text{Sm}^{3+}$ -doped ZnO compared to ZnO was attributed to the increase of separation of the photo-generated electrons and the photo-generated hole traps, producing more highly reactive  $\cdot\text{OH}$  and  $\cdot\text{O}_2$  radicals. Therefore, this simple route to produce higher-activity photocatalysts for environmental remediation of toxic compounds is shown to be cost-effective and to apply particularly in industrial production in the future.

**Acknowledgements** This paper was made possible by NPRP grant # 5-1425-2-607 and 7-1154-2-433 from the Qatar National Research Fund (a member of Qatar Foundation) and the Research Centre for Sustainable Process Technology (CESPRO), Faculty of Engineering and Built Environment, Universiti Kebangsaan Malaysia under project PKT-6/2012, iconic-2014-004. The statements made herein are solely the responsibility of the authors. One of the authors (Muneer M. Ba-Abbad) is grateful to Hadhramout University of Science & Technology, Yemen for its financial support for his PhD study. The authors would like to thank the Centre for Research and Instrumentation Management, UKM (CRIM) for XRD, FESEM, TEM and PL analyses. Special thanks to Dr. Ali Sardar from Gas Processing Centre (GPC), Qatar University, Qatar for the XPS analysis.

## Compliance with ethical standards

**Conflict of interest** The authors declare that they have no competing interests.

## References

1. John R, Rajakumari R (2012) Synthesis and characterization of rare earth ion doped nano ZnO. *Nano-Micro Lett* 4:65–72
2. Ong CB, Mohammad AW, Rohania R, Ba-Abbad MM, Hairom NHH (2016) Solar photocatalytic degradation of hazardous Congo red using low temperature synthesis of zinc oxide nanoparticles. *Process Saf Environ Prot* 104:549–557
3. Wang R, Xin JH, Yang Y, Liu H, Xu L, Hu J (2004) The characteristics and photocatalytic activities of silver doped ZnO nanocrystallites. *Appl Surf Sci* 227:312–317
4. Mohammed AJ, Kadhum AH, Ba-Abbad MM, Al-Amiery AA (2016) Optimization of solar photocatalytic degradation of chloroxylenol using  $\text{TiO}_2$ ,  $\text{Er}^{3+}/\text{TiO}_2$  and  $\text{Ni}^{2+}/\text{TiO}_2$  via taguchi orthogonal array technique. *Catalysts* 6:163–177
5. Du YP, Zhang YW, Sun LD, Yan CH (2008) Efficient energy transfer in monodisperse Eu-doped ZnO nanocrystals synthesized from metal acetylacetonates in high-boiling solvents. *J Phys Chem C* 112:12234–12241
6. Wang H, Dong S, Zhou X, Hu X, Chang Y (2011) Effect of synthesis conditions on microstructures and photoluminescence properties of Ga doped ZnO nanorod arrays. *Physica E* 44:307–312

7. Yu CL, Yang K, Yu J, Peng P, Cao F, Li X, Zhou XC (2011) Effects of rare earth Ce doping on the structure and photocatalytic performance of ZnO. *Acta Phys Chim Sin* 27:505–512
8. Gao S, Zhang H, Deng R, Wang X, Sun D, Zheng G (2006) Engineering white light-emitting Eu-doped ZnOurchins by biopolymer-assisted hydrothermal method. *Appl Phys Lett* 89:123–125
9. Mishra BG, Rao GR (2002) Promoting effect of CeO<sub>2</sub> on cyclohexanol conversion over CeO<sub>2</sub>-ZnO mixed oxide materials prepared by amorphous citrate process. *Bull Mater Sci* 25:155–162
10. Bastami H, Taheri-Nassaj E (2010) Synthesis of nanostructured (Co, Nb, Sm)-Doped SnO<sub>2</sub> powders using co-precipitation method. *J Alloys Compd* 495:121–125
11. Ba-Abbad MM, Takriff MS, Benamor A, Mohammad AW (2017) Size and shape controlled of  $\alpha$ -Fe<sub>2</sub>O<sub>3</sub> nanoparticles prepared via sol-gel technique and their photocatalytic activity. *J Sol-Gel Sci Technol* 81:880–893
12. Aydin C, Abd El-sadek MS, Zheng K, Yahia IS, Yakuphanoglu F (2013) Synthesis, diffused reflectance and electrical properties of nanocrystalline Fe-doped ZnO via sol-gel calcination technique. *Opt Laser Technol* 48:447–452
13. Lin CC, Young SL, Kung CY, HZ, Lance Horng MC, Chen K, Shih YT, Ou CR (2013) Phonon spectra and magnetic behaviors of hydrothermally synthesized Sm-doped ZnO nanorods. *Vacuum* 87:178–181
14. Jin CS, Sze ML, Keat TL, Abdul Rahman MJ (2013) Photocatalytic performance of novel samarium-doped spherical-like ZnO hierarchical nanostructures under visible light irradiation for 2,4-dichlorophenol degradation. *Colloid Interface Sci* 401:40–49
15. Jin CS, Sze ML, Keat TL, Abdul Rahman M (2013) Preparation and photocatalytic properties of visible light-driven samarium-doped ZnO nanorods. *Ceram Int* 39:5833–5843
16. Khatamian M, Khandar AA, Divbana B, Haghighb M, Ebrahimi S (2012) Heterogeneous photocatalytic degradation of 4-nitrophenol in aqueous suspension by Ln (La<sup>3+</sup>, Nd<sup>3+</sup> or Sm<sup>3+</sup>) doped ZnO nanoparticles. *J Mol Catal A: Chem* 365:120–127
17. Ba-Abbad MM, Kadhum AH, Mohamad AB, Takriff MS, Sopian K (2013) Optimization of process parameters using D-optimal design for synthesis of ZnO nanoparticles via sol-gel technique. *J Ind Eng Chem* 19:99–105
18. Ba-Abbad MM, Kadhum AH, Mohamad AB, Takriff MS, Sopian K (2013) The effect of process parameters on the size of ZnO nanoparticles synthesized via the sol-gel technique. *J Alloys Compd* 550:63–70
19. Al-Janabi KS, Alazawi FN, Mohammed MI, Kadhum AH, Mohamad AB (2012) Direct acetylation and determination of chlorophenols in aqueous samples by gas chromatography coupled with an electron-capture detector. *J Chromatogr Sci* 50:564–568
20. Ba-Abbad MM, Kadhum AH, Mohamad AB, Takriff MS, Sopian K (2013) Visible light photocatalytic activity of Fe<sup>3+</sup>-doped ZnO nanoparticles prepared via sol-gel technique. *Chemosphere* 91:1604–1611
21. Ni L, Wang L, Shao B, Wang Y, Zhang W, Jiang Y (2011) Synthesis of flower-like Zinc oxalate microspheres in ether-water bilayer refluxing systems and their conversion to zinc oxide microspheres. *J Mater Sci Technol* 27:563–569
22. Liu Y, Yang J, Guan Q, Yang L, Zhang Y, Wang Y, Feng B, Cao J, Liu X, Yang Y, Wei M (2009) Effects of Cr-doping on the optical and magnetic properties in ZnO nanoparticles prepared by sol-gel method. *J Alloys Compd* 486:835–838
23. Klug H, Alexander L (1962) X-ray diffraction procedure. Wiley, New York
24. Yang J, Li X, Lang J, Yang L, Wei M, Gao M, Liu X, Zhai H, Wang R, Liu Y, Cao J (2011) Synthesis and optical properties of Eu-doped ZnO nanosheets by hydrothermal method. *Mater Sci Semicond Process* 14:247–252
25. Tseng Y, Lin Y, Chang H, Chen Y, Liu C, Zou Y (2012) Effects of Ti content on the optical and structural properties of the Ti-doped ZnO nanoparticles. *J Lumin* 132:491–494
26. Faure B, Salazar AG, Ahniyaz A, Villaluenga I, Berriozabal G, Miguel YR, Bergström L (2013) Dispersion and surface functionalization of oxide nanoparticles for transparent photocatalytic and UV-protecting coatings and sunscreens. *Sci Technol Adv Mater* 14:023001–023024
27. Sehgal A, Lalatonne Y, Berret JF, Morvan M (2005) Precipitation-redispersion of cerium oxide nanoparticles with poly (acrylic acid): toward stable dispersions. *Langmuir* 21:9359–9364
28. Fissan H, Neumann S, Trampe A, Pui D, Shin WG (2007) Rationale and principle of an instrument measuring lung deposited nanoparticle surface area. *J Nano Res* 9:53–59
29. Weir A, Westerhoff P, Fabricius L, Hristovski K, Von Goetz N (2012) Titanium dioxide nanoparticles in food and personal care products. *Environ Sci Technol* 46:2242–2250
30. Nieto JJ, Freer D, Contreras RJ, Candal HD, Sileo M (2008) Photocatalyzed degradation of flumequine by doped TiO<sub>2</sub> and simulated solar light. *J Hazard Mater* 155:45–50
31. Ba-Abbad MM, Takriff MS, Benamor A, Mohammad AW (2016) Synthesis and characterization of Co<sup>2+</sup>-incorporated ZnO nanoparticles prepared through a sol-gel method. *Adv Powder Technol* 27:2439–2447
32. Yu X, Meng D, Liu C, He X, Wang Y, Xie J (2012) Structure and ferromagnetism of Fe-doped and Fe- and Co-codoped ZnO nanoparticles synthesized by homogeneous precipitation method. *Mater Lett* 86:112–114
33. Ba-Abbad MM, Takriff MS, Mohammad AW, Benamor A (2016) Size and shape controlled and magnetic properties of  $\alpha$ -Fe<sub>2</sub>O<sub>3</sub> nanoparticles prepared via sol-gel technique and their photocatalytic activity. *J Sol-gel Sci Technol* 81:881–893
34. Liu Y, Li R, Luo W, Zhu H, Chen X (2010) Optical spectroscopy of Sm<sup>3+</sup> and Dy<sup>3+</sup>-Doped ZnO nanocrystals. *Spectrosc Lett* 43:343–349
35. Nair MG, Nirmala M, Rekha K, Anukaliani A (2011) Structural, optical, photo catalytic and antibacterial activity of ZnO and Co doped ZnO nanoparticles. *Mater Lett* 65:1797–1800
36. Saifa M, Hafez H, Nabeel AI (2013) Photo-induced self-cleaning and sterilizing activity of Sm<sup>3+</sup>-doped ZnO nanomaterials. *Chemosphere* 90:840–847
37. Wang DD, Xing GZ, Yang JH, Yang LL, Gao M, Cao J, Zhang YJ, Yao B (2010) Dependence of energy transfer and photoluminescence on tailored defects in Eudoped ZnO nanosheets-based microflowers. *J Alloys Compd* 504:22–26
38. Dufour G, Karnatak RD, Mariot JM, Bonnelle C (1976) Atomic and chemical effects in Sm and Sm<sub>2</sub>O<sub>3</sub> photoelectron spectra. *Chem Phys Lett* 42:433–436
39. Thanh DN, Cao TD (2009) Monodisperse samarium and cerium orthovanadate nanocrystals and metal oxidation states on the nanocrystal surface. *Langmuir* 25:11142–11148
40. Ba-Abbad MM, Takriff MS, Mohammad AW (2016) Enhancement of 2-chlorophenol photocatalytic degradation in presence Co<sup>2+</sup>-doped ZnO nanoparticles under direct solar radiation. *Res Chem Intermed* 42:5219–5236
41. Paola AD, Bellardita M, Marci G, Palmisano L, Parrino F, Amadelli R (2011) Preparation of Sm-loaded brookite TiO<sub>2</sub> photocatalysts. *Catal Today* 161:35–40
42. Ba-abbad MM, Kadhum AH, Mohamad AB, Takriff MS, Sopian K (2013) Photocatalytic degradation of chlorophenols under direct solar radiation in the presence of ZnO catalyst. *Res Chem Intermed* 39:1981–1996

43. Abdel Aal A, Barakat MA, Mohamed RM (2008) Electrophoretic Zn–TiO<sub>2</sub>–ZnO nanocomposite coating films for photocatalytic degradation of 2-chlorophenol. *Appl Surf Sci* 254:4577–4583
44. Jafarzadeh NK, Sharifnia S, Hosseini SN, Rahimpour F (2011) Statistical optimization of process conditions for photocatalytic degradation of phenol with immobilization of nano TiO<sub>2</sub> on perlite granules. *Korean J Chem Eng* 28:531–538
45. Kaä RM, Andraä SF, Imre DK (2002) TiO<sub>2</sub>-based photocatalytic degradation of 2-chlorophenol adsorbed on hydrophobic clay. *Environ Sci Technol* 36:3618–3624
46. Rashid J, Barakat MA, Pettit SL, Kuhn JN (2004) InVO<sub>4</sub>/TiO<sub>2</sub> composite for visible-light photocatalytic degradation of 2-chlorophenol in wastewater. *Environ Technol* 35:2153–2159
47. Jamshaid R, Barakat MA, Ruzmanova Y, Chianese A (2015) Fe<sub>3</sub>O<sub>4</sub>/SiO<sub>2</sub>/TiO<sub>2</sub> nanoparticles for photocatalytic degradation of 2-chlorophenol in simulated wastewater. *Environ Sci Pollut Res* 22:3149–3157
48. Li N, Descorme C, Besson M (2007) wet air oxidation of 2-chlorophenol over Ru loaded Cex Zr1-xO2 solid solutions. *Appl Catal B* 76:92–100
49. Bandara J, Mielczarski JA, Lopez A, Kiwi J (2001) 2. Sensitized degradation of chlorophenols on iron oxides induced by visible light Comparison with titanium oxide. *Appl Catal B* 34:321–333